第33卷第6期
2014年12月

红外与毫米波学报
J. Infrared Millim. Waves

Vol. 33, No. 6
December, 2014

文章编号:1001 - 9014(2014)06 - 0577 - 07

DOI:10.3724/SP. J. 1010. 2014. 00577

High-resolution terahertz radar imaging based on electromagnetic calculation data

WANG Rui-Jun[1,2], WNAG Hong-Qiang[1*], DENG Bin[1], QIN Yu-Liang[1]

(1. School of Electronic Science and Engineering, National University of Defense Technology, Changsha 410073, China;
2. 95876 Air Force Troops PLA, Shandan 734100, China)

Abstract: In order to reveal the scattering characteristics of targets at terahertz frequencies, high resolution radar imaging was studied based on the high frequency (HF) electromagnetic calculation data. Considering huge data flow of 3D image formation, a novel azimuth-elevation imaging theory with its result similar to a photograph of targets was proposed. The point spread function is derived for revealing the high resolution performance and scatterers identification capability. Simulation results demonstrated that HF method can solve radar cross section of perfectly electrical conducting (PEC) target accurately and fast at terahertz frequencies. The high resolution images show that the sub-wavelength features of targets are resolvable. It also implies that terahertz radar can attain more fine information about targets, which will be helpful for target recognition.

Key words: terahertz, radar imaging, high frequency method, radar cross section
PACS: 84.40.Xb, 42.30.Va, 41.20.-q

基于高频电磁计算数据的太赫兹雷达高分辨成像研究

王瑞君[1,2], 王宏强[1*], 邓 彬[1], 秦玉亮[1]

(1. 国防科技大学 电子科学与工程学院,湖南 长沙 410073;
2. 空军95876部队,甘肃 山丹 734100)

摘要:为揭示太赫兹频段雷达目标散射特性,基于高频电磁计算数据研究了太赫兹雷达高分辨成像方法.考虑到传统三维雷达成像面临的大数据量问题,提出了一种成像结果类光学图像的高分辨成像方法——方位/俯仰成像方法,通过推导其点扩展函数分析了该方法在高分辨率与散射点识别方面的优势.基于电磁计算数据的仿真与分析表,高频计算方法可以快速准确计算太赫兹频段理想导体目标RCS,高分辨成像结果可以分辨目标亚波长量级的细微结构特征.因此太赫兹雷达成像技术可获取目标更加丰富和精细的信息,为目标识别带来益处.

关 键 词:太赫兹;雷达成像;高频方法;雷达散射截面

中图分类号:TN958 **文献标识码**:A

Introduction

Over the past several years, there has been a significant interest in applying terahertz (THz) sensing and imaging techniques into defense, security, and medicine[1-2]. As a fundamental research subject of terahertz science and technology, the interaction between THz wave and objects is frequently discussed[3-5]. When the object is illustrated by THz wave, its backscattering behavior will show difference compared with that in microwave or infrared spectrum region[6]. Currently, terahertz scattering from objects or targets is studied mainly based on computational electromagnetic simulation and experiment measurement. Some research literatures pointed out that HF asymptotic methods can be employed in solving computational electromagnetic problems at terahertz frequencies[7], and the reliability of this method has been

Received date: 2013 - 07 - 04, **revised date**: 2014 - 10 - 08 **收稿日期**:2013 - 07 - 04, **修回日期**:2014 - 10 - 08
Foundation items: Supported by National Science Fund (61171133), and National Natural Science Foundation for Young Scientists of China (61101182, 61302148)
Biography: WANG Rui-Jun(1986-), male, Inner Mongolian, China, Ph. D. Candidate, Research fields focus on radar imaging and scattering characteristics of targets at terahertz frequencies. E-mail: wandering_jun@163.com
* **Corresponding author**: E-mail: oliverwhq1970@gmail.com

verified by experimental results[8-10]. During past several years, many research institutions also have built different types of terahertz experiment systems for parameter measurement such as reflection spectra, RCS so on[11-13]. However, the measured data above does not provide a detailed description of terahertz scattering phenomena, and a more descriptive approach can be helpful for understanding the existing theories. Imaging techniques have been widely used in other areas of electromagnetic as a tool for analysis and understanding of scattering and propagation phenomena. For example, studies of natural target scattering have used high-resolution radar images to examine small foliage targets[14]. Imaging techniques to assist in separating different parts of the target are also of interest in space target recognition[15-16]. Study of scattering characteristic of the target at terahertz frequencies based on radar imaging will be meaningful for understanding scattering mechanism and establishing its scattering model.

For terahertz radar, its carrier frequency is very high. Wideband signals can be more easily transmitted. The range resolution which is inversely proportional to the bandwidth can be improved. On the other hand, higher radar frequencies can result in high cross-range resolution with relatively small angular apertures according to inverse synthetic aperture radar (ISAR) principle. Taking into account the target's complex structures that is comparable with wavelength, terahertz imaging radar can give the high resolution image of the target which includes the components of detailed scattering. It exhibits that radar imaging technique has great advantage for scattering characteristic analysis of targets.

In this paper, high resolution radar imaging of targets at terahertz frequencies is investigated based on HF asymptotic method calculation data. In section 1, the 3D imaging model and the imaging algorithm are established firstly. Considering the problem of huge data acquisition for 3D imaging, a novel azimuth-elevation imaging method is proposed. In section 2, the realization of HF asymptotic method is performed and the correctness of shooting and bouncing ray (SBR) method at terahertz frequencies is verified. In section 3, 3D and 2D imaging results for different targets are given and compared, including a discussion of the terahertz radar imaging. The conclusion is presented in section 4.

1 Radar imaging theory

1.1 Three-dimensional imaging geometry

Three-dimensional radar imaging model were built based on ISAR imaging principle, and the relationship between the scattering fields and target's 3D reflectivity distribution was given exactly.

As shown in Fig. 1, when the target coordinate system OXYZ is fixed, the unit vector of the radar line of sight (LOS) which points from the radar to the origin O can be expressed as $(\cos\theta\cos\varphi, \cos\theta\sin\varphi, \sin\theta)$. θ and φ denote the azimuth and elevation angle of the radar. In far-field region, the electromagnetic wave both illuminated on the target and returned from the target can be treated as the plane wave. The radar echo of scatterer P can be expressed as

$$r(k,\theta,\varphi) = S_p \cdot \exp(-j2\pi k R_d) \quad , \quad (1)$$

where $R_d = R_p - R_0 \approx <\mathrm{P}, \mathrm{LOS}>$ and $<\cdot>$ denotes vector multiplication. R_p and R_0 denote the distance from the radar to P and O. S_p is the intensity of P. $k = 2(f_0 + \gamma t)/c$ is the wave-number. c and t denote the velocity of light and fast time, respectively.

When there are large amounts of scatterers on the target, $g(x,y,z)$ is employed in depicting the 3D reflectivity distribution of the target. The coherent radar echo at arbitrary view angle can be rewritten as

$$r(k,\theta,\varphi) = \iiint_{x\,y\,z} g(x,y,z)\exp(-j2\pi (x\cdot k_x + y\cdot k_y + z\cdot k_z))\,\mathrm{d}x\mathrm{d}y\mathrm{d}z \quad , \quad (2)$$

where the wave-number domain vectors satisfy $k_x = k\cos\theta\cos\varphi$, $k_y = k\cos\theta\sin\varphi$, $k_z = k\sin\theta$.

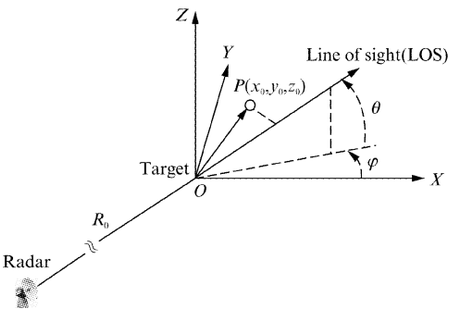

Fig. 1 Diagram of three-dimensional radar imaging
图1 雷达三维成像几何示意图

According to Eq. 2, the reflectivity distribution function can be obtained by performing a 3D inverse Fourier transform.

$$g(x,y,z) = \iiint_{k\,\theta\,\varphi} k^2\cos\theta \cdot r(k,\theta,\varphi) \cdot \exp(j2\pi(xk_x + yk_y + zk_z))\,\mathrm{d}k\mathrm{d}\theta\mathrm{d}\varphi \quad . \quad (3)$$

The above equation describes the relationship between wave-number domain samples and image for 3D imaging. Data collection in wave-number domain is related to the selection of azimuth angles, elevation angles and range of sweep frequencies. In order to facilitate ISAR imaging, the relationship of 3D imaging is transformed from the target-fixed coordinates to the radar-fixed coordinates. Assuming that the radar-fixed coordinates is consistent with the target-fixed coordinates when the LOS is in the opposite direction of X, then the coordinate transformation can be viewed as a 2D rotation by the center azimuth and elevation angles, i. e. θ_c and φ_c. The transformation matrix and the reflectivity distribution function of target in radar-fixed coordinates can be expressed as

$$T = \begin{bmatrix} \cos\varphi_c\cos\theta_c & \sin\varphi_c\cos\theta_c & \sin\theta_c \\ -\sin\varphi_c & \cos\varphi_c & 0 \\ -\cos\varphi_c\sin\theta_c & -\sin\varphi_c\sin\theta_c & \cos\theta_c \end{bmatrix} , \quad (4)$$

$$g(x',y',z') = \iiint_{k\,\theta\,\varphi} k^2\cos\theta \cdot r(k,\theta,\varphi) \exp(j2\pi(x'k_{x'} + y'k_{y'} + z'k_{z'}))\,\mathrm{d}k\mathrm{d}\theta\mathrm{d}\varphi \quad , \quad (5)$$

where the wave-number domain vectors $k_{x'}$, $k_{y'}$ and $k_{z'}$ are given as

$$\begin{aligned} k_{x'} &= k(\cos\theta\cos\theta_c\cos(\varphi-\varphi_c)+\sin\theta\sin\theta_c) \\ k_{y'} &= k\cos\theta\sin(\varphi-\varphi_c) \\ k_{z'} &= k(-\cos\theta\sin\theta_c\cos(\varphi-\varphi_c)+\sin\theta\cos\theta_c) \end{aligned} \quad . (6)$$

As depicted in Eq. 6, data collection aperture in target-fixed wave-number coordinates is shown in Fig. 2, which is presented as a part of sphere grid. Application of a Fourier transform to the samples of the target's wave-number domain collection data produces a reconstruction of the target's 3D reflectivity distribution. In the interest of computational efficiency, the target's image reconstruction is carried out by first performing a 3D interpolation of the data samples onto a 3D Cartesian grid. Then, a 3D fast Fourier transform (FFT) process is applied to the interpolated samples to form the target's image. Since image formation is closely related to the Fourier transform, there is a tradeoff between side-lobe level and spatial resolution. Windows functions in both frequency and angle are chosen to set the relationship between these quantities. In this paper, the well-known Taylor window is selected, resulting in a fast decaying side-lobe level at the expense of degrading of image resolution.

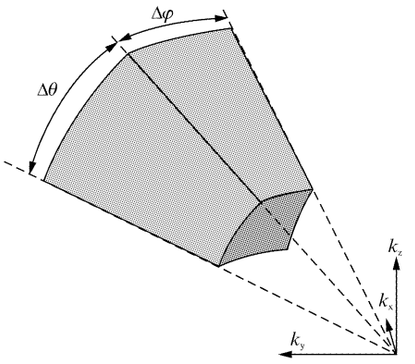

Fig. 2　3D data collection aperture in target-fixed wave-number coordinates

图 2　目标波束域坐标系中的三维数据采集孔径

1.2　THz azimuth-elevation imaging

The 3D radar imaging requires data collection of wide-band and wide angle with small increment, leading to a huge data flow and computational load. Thus it hinders the scattering diagnose by experimental measurement or numerical simulation data at terahertz frequencies. For Eq. 5, if the single frequency signal is launched and the rotated target forms an aperture in azimuth and elevation direction, a 2D azimuth-elevation image can be obtained by performing a Fourier transform to less complex RCS data. The point spread function (PSF) determines the resolution performance of THz azimuth-elevation imaging. According to Eq. 5, the PSF with single frequency and arbitrary rotated angles can be expressed as

$$\rho(x',y',z') = \iint_{\theta\varphi} k_0^2\cos\theta\exp(j2\pi (x'k_{x'}+y'k_{y'}+z'k_{z'}))\,\mathrm{d}\theta\mathrm{d}\varphi \quad . (7)$$

The PSF is totally determined by the integral in the azimuth and elevation aperture. In the case of imaging with small angle of rotation, it's deemed that the following assumption is satisfied: $\cos(\theta-\theta_c)=1$, $\sin(\theta-\theta_c)=\theta-\theta_c$, $\cos(\varphi-\varphi_c)=1$, $\sin(\varphi-\varphi_c)=\varphi-\varphi_c$. Therefore, the PSF can be simplified as

$$\begin{aligned} \rho(x',y',z') &= \iint_{\theta\varphi} k_0^2\cos\theta\cdot\exp(j2\pi k_0(x'+y'(\varphi-\varphi_c)\cos\theta+z'(\theta-\theta_c)))\,\mathrm{d}\varphi\mathrm{d}\theta = \\ & k_0^2\exp(j2\pi k_0x')\frac{1}{\pi k_0y'}\int_{\theta_c-\frac{\Delta\theta}{2}}^{\theta_c+\frac{\Delta\theta}{2}}\exp(j2\pi k_0z'(\theta-\theta_c))\cdot \\ & \sin(\Delta\varphi\pi k_0y'\cos\theta)\,\mathrm{d}\theta \end{aligned} \quad . (8)$$

When $\Delta\varphi$ and y' are very small, $\sin(\Delta\varphi\pi k_0 y'\cos\theta)\cong\Delta\varphi\pi k_0y'\cos\theta$ is true and its value is almost a constant although the elevation angle θ is variable around θ_c. So the PSF can be rewritten as

$$\begin{aligned} \rho(x',y',z') &= k_0^2\exp(j2\pi k_0x')\frac{\sin(\Delta\varphi\pi k_0 y'\cos\bar{\theta})}{\pi k_0y'} \\ & \int_{\theta_c-\frac{\Delta\theta}{2}}^{\theta_c+\frac{\Delta\theta}{2}}\exp(j2\pi k_0z'(\theta-\theta_c))\,\mathrm{d}\theta = k_0^2\exp(j2\pi k_0x')\cdot \\ & \Delta\varphi\cdot\Delta\theta\cdot\mathrm{sinc}(\Delta\varphi\pi k_0 y'\cos\bar{\theta})\cdot \\ & \mathrm{sinc}(\Delta\theta\pi k_0z') \end{aligned} \quad . (9)$$

In order to obtain the resolutions of azimuth-elevation imaging, three different sections of PSF are given in the following

$$\begin{aligned} \rho(x',0,0) &= k_0^2\cdot\exp(j2\pi k_0x')\cdot\Delta\theta\cdot\Delta\varphi \\ \rho(0,y',0) &= k_0^2\cdot\Delta\theta\cdot\Delta\varphi\cdot\mathrm{sinc}(\Delta\varphi\pi k_0 y'\cos\bar{\theta}) \\ \rho(0,0,z') &= k_0^2\cdot\Delta\theta\cdot\Delta\varphi\cdot\mathrm{sinc}(\Delta\theta\pi k_0z') \end{aligned} \quad . (10)$$

It can be seen that there is no resolving power in the x' direction corresponding to range resolution. In the y' and z' direction, azimuth and elevation resolutions are determined by the position of the first zero point of sinc function.

$$y_{\mathrm{pn}} = \delta_{\mathrm{Azi}} = \frac{\lambda}{2\Delta\varphi\cos\bar{\theta}}, z_{\mathrm{pn}} = \delta_{\mathrm{Ele}} = \frac{\lambda}{2\Delta\theta} \quad . (11)$$

Azimuth resolution is related to the elevation angle of LOS in target-fixed coordinates, while elevation resolution is identical to cross-range resolution of ISAR. As shown in Fig. 2, the total span $\Delta\varphi$ in azimuth angle depicts only the size of the aperture in k_x-k_y plane. When the elevation angle is increased, the actual span in azimuth angle becomes small gradually, which resulting in degrading of the azimuth resolution. However there is still a great advantage of high cross-range resolution for the method while only small rotation angles are required. For lower frequency radar, the required rotation angles become much large when the same resolutions are achieved, and the situation of large rotation angles both in azimuth and elevation directions is barely satisfied simultaneously.

The method obtains the target's image in 2D Doppler plane and the formed image shows the target in the same perspective as it is illuminated. In this respect, the azimuth-elevation image is similar to a photograph of the target, which makes identification of individual scattering centers much easier. In contrast, for the range-Doppler method of microwave radar the range information comes from a direction that is parallel to the radar line of sight, and this leads to top down image being formed for a target. Since there is no elevation information and it results

in ambiguity in identification of individual scatterers. Additionally, due to the observation of small angles and the reflectivity distribution of 2D Doppler plane, the proposed imaging method is barely influenced by the truth of aspect sensitivity or anisotropic scattering of the target, while it is worse for microwave radar on condition of large rotation angles.

2 Realization of high frequency method

The SBR technique is a standard ray tracing technique for predicting the scattering from complex electrically large targets. The accuracy of SBR prediction in microwave bands has been extensively tested in the past, including comparison against numerical Maxwell's solvers and experimental data[18]. At the lower terahertz frequencies, metallic targets can still be treated as perfect electrical conductor. In the following, the SBR technique is adopted for solving target's RCS at terahertz frequencies, and the SBR prediction result is compared with the numerical result of multilevel fast multipole algorithm (MLFMA), which try to verify the accuracy of the SBR method at terahertz frequencies.

Solving scattering problem of target using SBR method includes three steps. Firstly, given target's geometrical CAD model and incident field, find the ray paths on the target by ray tracing. This part of problem is dependent only on the geometry of the target, and can be solved according to Snell's law. Secondly, determine the field amplitude of the exit rays on the aperture based on geometrical optics. Thirdly, obtain the outgoing field on the aperture and use physical optics to determine the backscattered field and the RCS of each raytube. Then sum all the contribution of each raytube, and the total backscattered field can be expressed as

$$\vec{E}_s = -jkZ_0\psi_0 \sum_{n=1}^{N} \left(\int_{S_n} \hat{s} \times [\hat{s} \times (2\hat{n} \times \vec{H}_i)] \exp(-jk\vec{r}' \cdot (\hat{i} - \hat{s})) \mathrm{d}S_n \right) \quad , \quad (12)$$

where N is the number of raytubes, $\vec{H}_i$ is the incident magnetic current, ψ_0 is the far-field Green function, $\hat{i}$ and $\hat{s}$ are incident and scattering vector, respectively.

Figure 3 is the simulation results of a cylinder conductor at 340 GHz, which give the amplitude and phase of monostatic RCS with different incident angles. At the same time, the SBR results were compared with MLFMA results, and excellent agreement in the RCS computation

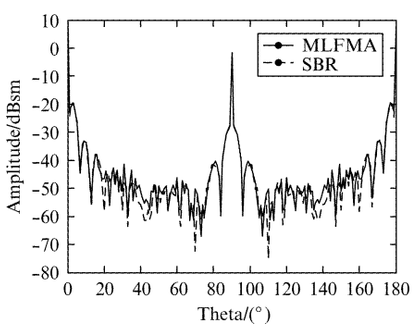

(a)

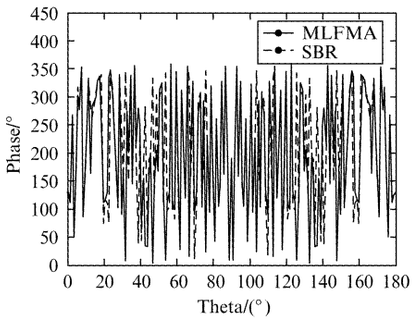

(b)

Fig. 3 Comparison of monostatic VV RCS for a cylinder conductor with dimension $h = 8$ cm, $r = 1.5$ cm (a) Amplitude, and (b) phase

图3 SBR方法与MLFMA方法分别预测的圆柱导体VV极化RCS结果比较 (a)幅度, (b)相位

was observed. A few of errors exist in some incident angles because the SBR ignores such effects as surface waves, higher-order diffraction, and diffraction-reflection in its basic form. On the other hand, SBR method eliminates lots of time compared with the MLFMA, while obtaining nearly the same result.

3 Simulations and analysis

3.1 Three-dimensional imaging results

As shown in Fig. 4, a warhead model and a T62 tank model were used for investigating their 3D imaging characteristics at terahertz frequencies. The warhead with four wings is 60 cm in length and 26 cm in base diameter, while the T62 model is circumscribed onto a 24 cm × 8.4 cm × 7.9 cm Cartesian grid. The imaging of the two targets were performed in a frequency range from 320 GHz to 350 GHz at different azimuth and elevation angles.

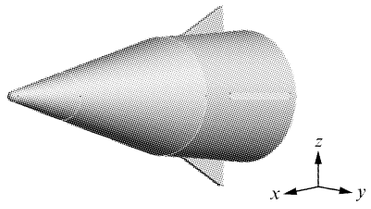

(a)

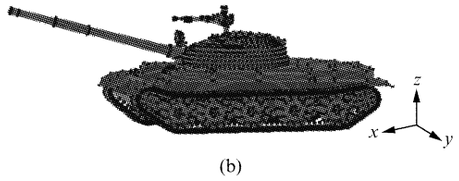

(b)

Fig. 4 (a) Warhead model with cross-range aperture $\Delta\varphi = -3.15° \sim 3.15°$, $\Delta\theta = -3.15° \sim 3.15°$, (b) T62 tank model with cross-range aperture $\Delta\varphi = 71.85° \sim 78.15°$, $\Delta\theta = 1.85° \sim 8.15°$

图4 (a)弹头模型,方位观测孔径为 $\Delta\varphi = -3.15° \sim 3.15°$, $\Delta\theta = -3.15° \sim 3.15°$, (b)T62坦克模型,方位观测孔径为 $\Delta\varphi = 71.85° \sim 78.15°$, $\Delta\theta = 1.85° \sim 8.15°$

The vertical-transmit/vertical-receive (VV) imaging results of the warhead model are plotted over 6.3° × 6.3° solid view angle using a 0.03° angular increment in Fig. 5. For understanding the scattering characteristics of targets, projections of 3D reflectivity distribution in different coordinate plane are shown first when referenced to the radar-fixed coordinate system. The $X'-Z'$ projection represents the front aspect view of the 3D reflectivity distribution at 0° azimuth/elevation view angle, the $Y'-Z'$ projection represents the side aspect view at 90° azimuth and 0° elevation view angle, while the $X'-Y'$ projection represents the top aspect view at 0° azimuth and 90° elevation view angle. In order to compare with the warhead model, Fig. 5(d) displays the 3D reflectivity distribution in the target-fixed coordinate system and the aspect angle is at 80° azimuth and 90° elevation view angle. The top, wings, bottom and discontinuity edge of the warhead can be clearly seen. Because of the wide view aperture, the bottom and discontinuity edge of warhead forms the slide scattering centers, which is presented as parts of circle. Meanwhile, VV polarization decided that the arc can't become closed circle and two wing scattering center are only observed. However we can still identify warhead's outline easily from the 3D imaging results.

The 3D imaging results of T62 tank model in VV polarization are given in Fig. 6. The wideband data was collected over 6.3° × 6.3° solid angle using a 0.05° angular increment. For each projection of 3D reflectivity distribution in different coordinate plane, it reflects the outline of the T62 tank and distribution of scatterers on it. The 3D imaging results in target-fixed coordinate system is showed at 75° azimuth and 5° elevation in Fig. 6 (d). It is evident that 3D imaging results shows detailed scattering information on target with very small features being seen, especially for the wheel and turret. The imaging resolution is nearly to be 5 mm, which verifies acquisition ability of high resolution image of complex target at terahertz frequencies.

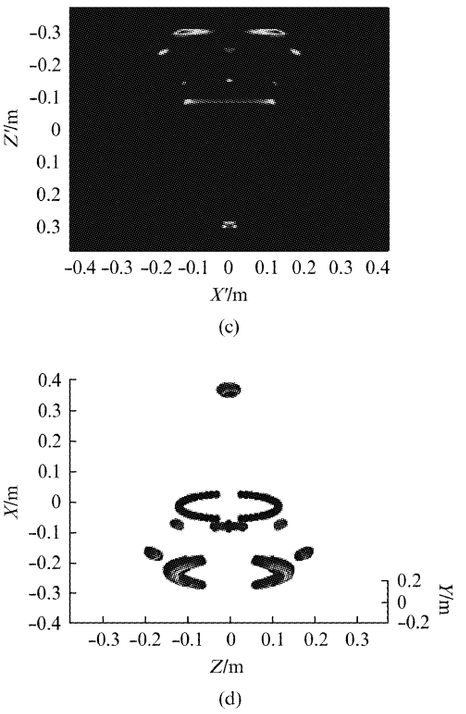

Fig. 5 Imaging results of warhead referenced to the radar-fixed coordinate system (a) Y'-Z' projection, (b) X'-Y' projection, (c) X'-Z' projection, and (d) 3D reflectivity distribution referenced to the target-fixed coordinate system

图 5 雷达坐标系下的立方体三维 VV 成像结果(a) Y'-Z'平面投影,(b) X'-Y'平面投影,(c) X'-Z'平面投影,(d) 目标坐标系中三维散射分布

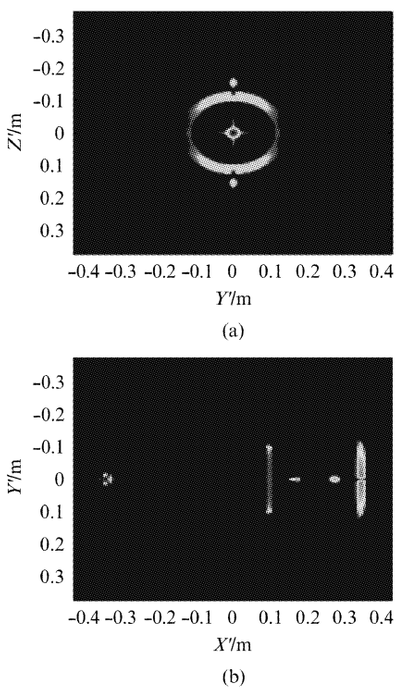

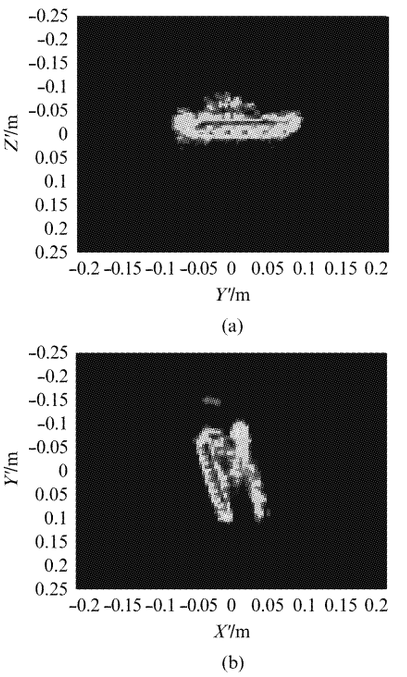

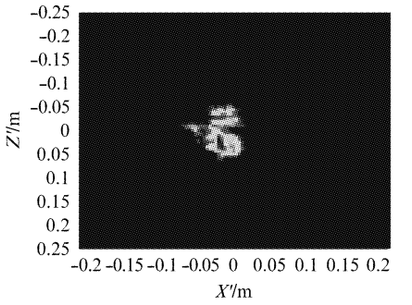

(c)

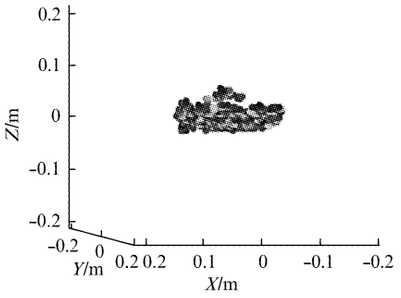

(d)

Fig. 6 Imaging results of T62 referenced to the radar-fixed coordinate system (a) Y'-Z' projection, (b) X'-Y' projection, (c) X'-Z' projection, and (d) 3D reflectivity distribution referenced to the target-fixed coordinate system

图6 雷达坐标系下的T62坦克三维VV成像结果(a) Y'-Z'平面投影,(b) X'-Y'平面投影,(c) X'-Z'平面投影,(d) 目标坐标系中三维散射分布

3.2 Azimuth-Elevation imaging results

Using the azimuth-elevation imaging technique that is described in Section 1.3, targets' 2D imaging results are given in the following. Figure 7 gives azimuth-elevation imaging results of the warhead in VV polarization at different azimuth angles. It was observed that the warhead model in Fig. 7(a) is modified by adding four gesture-controlled holes of that showed in Fig. 4(a). Single frequency RCS data is collected over 5° ×5° solid angle using a 0.03° angular increment when the carrier frequency is 340 GHz. Figure 7(b)(c) are images of the warhead at 75° elevation and different azimuth angle, 0° and 45°, respectively. This method produced 2D images with 5 mm elevation resolution and 19.5 mm azimuth resolution, which results from a large elevation angle. From the view angle as target is illuminated, the main scatterers such as top, wings, holes, bottom and discontinuity edge are clearly distinguishable. The outline of the warhead can also be easily identified.

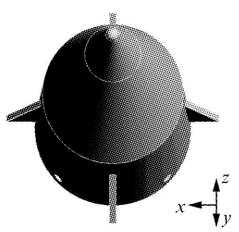

(a)

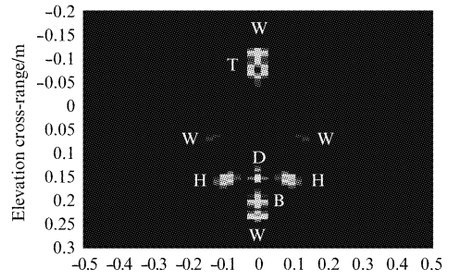

(b)

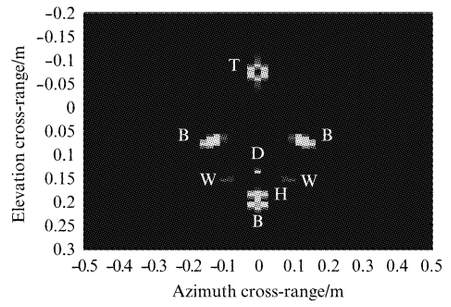

(c)

Fig. 7 Azimuth-Elevation images of warhead. (a) Photograph of model, (b) image 0° azimuth, (c) image at 45° azimuth. (W: wing, T: top, H: hole, B: bottom, D: discontinuity)

图7 弹头目标的方位俯仰成像(a) 模型图,(b) 方位角0°时成像,(c) 方位角45°时成像(W: 尾翼, T: 顶部, H: 孔, B: 底端, D: 不连续处)

Azimuth-Elevation images of T62 tank at 340 GHz and 675 GHz is given in Fig. 8 based on data collected over 5° × 5° solid angle, which achieve 4mm and 2mm cross-range resolution, respectively. The images not only give the outline of tank, but also exhibit the detailed scattering features such as wheel and turret. When the single frequency is 675 GHz, the imaging result becomes more clearly and similar to a photograph of the target. However the tank's barrel was not observed due to non-perpendicular of LOS to the cylindrical barrel. Fig. 9 shows the azimuth-elevation image of another tank model in VV polarization at 40° elevation and 0° azimuth view angle when carrier frequency is 340 GHz, the figures also show a photograph of model at the same azimuth and elevation view angle. It is evident that azimuth-elevation imaging results show the wheel、turret and barrel of tank clearly. This imaging technique is very useful in identifying individual scatterers on a target and identifying problems with the field-of-view of the system.

4 Conclusions

High resolution radar imaging of targets at terahertz frequencies was studied based on electromagnetic calculation data. The SBR technique is proved to be an effective method for predicting the scattering of complex electrically large conductor targets at terahertz frequencies. The 3D imaging and azimuth-elevation imaging methods presented in this paper are very useful for investigating imaging characteristics of radar targets at terahertz frequencies. The 3D and 2D images of several different targets

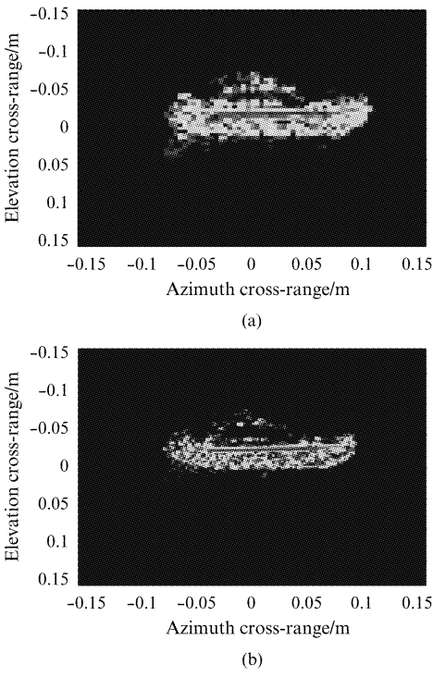

Fig. 8　Azimuth-Elevation images of T62 at 5° elevation and 75° azimuth when carrier frequencies are (a) 340 GHz, and (b) 675 GHz

图 8　俯仰 5°和方位 75°时不同载频下的 T62 坦克方位俯仰成像 (a) 载频 340 GHz,(b) 载频 675 GHz

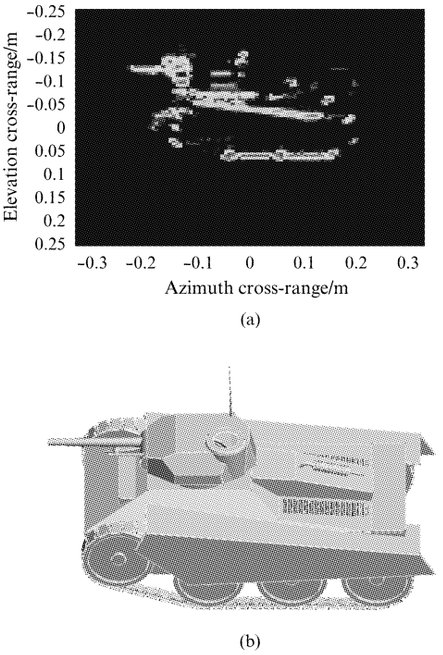

Fig. 9　(a) Azimuth-Elevation image of the Tank, and (b) photograph of the tank model

图 9　(a)坦克模型的方位俯仰成像,(b)坦克模型图

show the ability of high resolution imaging with several millimeter resolutions, which gives detailed scattering features on target. For the target with complex surface structure the azimuth-elevation image is similar to a photograph of the target. The imaging technique has been proven useful in identifying individual scattering centers on targets.

References

[1] Liu H B, Zhong H, Karpowicz N, *et al*. Terahertz spectroscopy and imaging for defense and security applications[J]. *Proceedings of the IEEE*, 2007, **95**(8): 1514-1527.

[2] Withayachumnankul W, Peng G M, Yin X X, *et al*. T-Ray sensing and imaging[J]. *Proceedings of the IEEE*, 2007, **95**(8): 1528-1558.

[3] Sundberg G, Zurk L M, Schecklman S, *et al*. Modeling rough-surface and granular scattering at terahertz frequencies using the finite-difference time-domain method[J]. *IEEE Transactions on Geoscience and Remote Sensing*, 2010, **48**(10): 3709-3719.

[4] Jagannathan A, Gatesman A J, Horgan T, *et al*. Effect of periodic roughness and surface defects on the terahertz scattering behavior of cylindrical objects[C]. *Proceedings of the SPIE*, 2010: 7671.

[5] Zurk L M, Orlowski B, Sundberg G, *et al*. Electromagnetic scattering calculations for terahertz sensing[C]. *Proceedings of SPIE*, 2007: 6472.

[6] Siegel P H. Terahertz technology[J]. *IEEE Transactions on Microwave Theory and Techniques*, 2002, **50**(3): 910-928.

[7] Li Z, Cui T J, Zhong X J, *et al*. Electromagnetic scattering characteristics of PEC targets in the terahertz regime[J]. *IEEE Antennas and Propagation Magazine*, 2009, **51**(1): 39-50.

[8] Lonnqvist A, Mallat J, Raisanen A V. Phase-hologram-based compact RCS test range at 310 GHz for scale models[J]. *IEEE Transactions on Microwave Theory and Techniques*, 2006, **54**(6): 2391-2397.

[9] Gente R, Jansen C, Geise R, *et al*. Scaled bistatic radar cross section measurements of aircraft with a fiber-coupled THz time-domain spectrometer[J]. *IEEE Transactions on Terahertz Science and Technology*, 2012, **2**(4): 424-431.

[10] Iwaszczuk K, Heiselberg H, Jepsen P U. Terahertz radar cross section measurements[J]. *Optics Express*, 2010, **18**(25): 26399-26408.

[11] Gatesman A J, Danylov A, Goyette T M, *et al*. Terahertz behavior of optical components and common materials[C]. *Proceedings of the SPIE*, 2006: 6212.

[12] Jagannathan A, Gatesman A J, Giles R H. Characterization of roughness parameters of metallic surfaces using terahertz reflection spectra [J]. *Optics Letters*, 2009, **34**(13): 1927-1929.

[13] CHEN L-Qun, GAO Fei, GONG Xiao-Jing, *et al*. Extraction of refractive indices of materials through transmission terahertz time-domain spectroscopy[J]. *J. of Infrared Millim. Waves*(陈立群, 高飞, 龚小竞, 等. 一种利用透射式太赫兹时域光谱技术精确提取样品折射率的方法. **红外与毫米波学报**), 2013, **32**(2): 160-164.

[14] Kim H, Johnson J T, Baertlein B, *et al*. High resolution Ka-band backscatter images of a small tree: Measurements and models[J]. *IEEE Transactions on Geoscience and Remote sensing*, 2000, **38**(2): 899-910.

[15] Wang Q, Xing M D, Lu G Y, *et al*. High-resolution three-dimensional radar imaging for rapidly spinning targets[J]. *IEEE Transactions on Geoscience and Remote sensing*, 2008, **46**(1): 22-30.

[16] Danylov A A, Goyette T M, Waldman J, *et al*. Terahertz inverse synthetic aperture radar (ISAR) imaging with a quantum cascade laser transmitter[J]. *Optics Express*, 2010, **18**(15): 16264-16272.

[17] Kim H, Johnson J T. Radar images of rough surface scattering comparison of numerical and analytical models[J]. *IEEE Transactions on antennas and propagation*, 2002, **50**(2): 94-100.